Analysis of Microstructure and Mechanical Properties of AZ31B Magnesium Alloy/AA6061 Aluminum Alloy Welded Joint by Ultrasonic Welding

Zhanzhan Su[a] (iD) *, Zhengqiang Zhu[a]** (iD) *, Yifu Zhang[a,b]* (iD) *, Hua Zhang[a]* (iD)

[a]Nanchang University, School of Mechanical & Electrical Engineering, Key Laboratory for Robot & Welding Automation of Jiangxi Province, Nanchang, 330031, China
[b]Jiujiang University, School of Mechanics & Materials Engineering, Jiujiang, 332005, China

AZ31B magnesium alloy/AA6061 aluminium alloy welded structures have been widely used in the lightweight design of automobile bodies. To improve the joint strength, the ultrasonic spot welding (USW) solid state connection method is used in this paper. The results show that at a welding energy of 1540 J, there is evidence of melting in the weld joint. As the welding energy increases, the intermetallic compounds (IMCs) grow rapidly and form a reaction layer approximately 17 μm thick. The IMCs are mainly composed of the γ-$Mg_{17}Al_{12}$+β-Mg_2Al_3 phase, where the β-Mg_2Al_3 phase hardness is as high as 6.5 GPa and shows a typical pop-in phenomenon and the average hardness of the γ-$Mg_{17}Al_{12}$ cubic structure phase is 3.4 GPa. When the welding energy reaches 1540 J, the β phase rapidly grows, and the joint performance decreases rapidly. The fracture morphology indicates a cleavage fracture and is accompanied by a large number of secondary cracks.

Keywords: AZ31B magnesium alloy/AA6061 aluminium alloy, ultrasonic spot welding (USW), intermetallic compounds (IMCs), pop-in phenomenon, joint performance.

1. Introduction

In many engineering applications, multiple material structures are more efficient and perform better than the same structure produced from a single material. An important emerging example is transportation. Replacing the overall steel structure with a variety of materials consisting of aluminium alloy/magnesium alloys can greatly reduce vehicle weight and improve fuel efficiency[1-3]. Ultrasonic spot welding (USW) technology enables rapid metallurgical bonding between metal layers by ultrasonic friction at only 25% ~ 70% of the melting point. This technique avoids liquid-solid phase transition, residual stress, dimensional change and metallurgical incompatibility; minimizes the time for formation of brittle intermetallic compounds (IMCs); and is a solid-state joining process with low heat input[4-6]. At the same time, this method is easy to automate. USW provides a solution for the connection of difficult-to-weld materials such as steel, magnesium alloy and aluminium alloy dissimilar materials. Due to the lower temperature and lack of a liquid phase, fewer IMCs are produced than in the fusion process. However, when these metals contact and diffuse into each other, an IMC reaction layer is still formed[7-10]. The growth rate is very fast, which is attributed to the abnormally rapid spread of interface IMCs, but the origin of this behaviour is not clear. The cracks tend to spread through the IMC layer, resulting in dissimilar metal joints with worse mechanical properties, especially fracture energy. The IMC layer is still critical in determining weldability.

Domestic and foreign scholars have conducted related experimental research on and established theoretical models of the ultrasonic welding of different metal materials. The effects of different welding processes on the microstructure and properties of welded joints were studied. The growth model of IMCs in ultrasonic welding was established, and the importance of IMCs in the joint strength was determined. For example, Zhu et al.[11] conducted an experimental study on aluminium alloy/titanium alloy USW, optimized the welding process parameters (welding pressure of 0.4mpa, welding time of 170ms) and obtained the maximum shearing force of 150N. After welding,The hardness of the welded joint is higher than that of the base metal, especially in the region around the bonding surface. As the welding time increases, the width of the diffusion zone gradually increases. Watanabe et al.[12] studied SS400 low carbon steel/A5052 aluminium alloy USW. The results show that the joint strength reaches 700N when the clamping force is 588N and the welding time is 2.5s. Due to the excessively large clamping force will reduce the frictional action at the interface, and too long welding time will cause the formation of Fe_2Al_5 IMC at the interface, which will reduce the joint strength. When the clamping force is 588N and the welding time is 3s, Using the insert metal of A1050 pure aluminum successfully improved the joint strength and the joint strength reaches nearly 2000N. This is because the little amount of Mg contained in pure aluminum effectively prevents the formation of Fe_2Al_5 IMC at the interface. Panteli et al.[13] studied the relationship between USW interfacial reaction and welding energy of aluminium AA6111-T4 / magnesium AZ31-H24 alloy sheets with a thickness of 1mm.

*e-mail: zhuzq_lab@163.com

The results show that a continuous layer composed of two sub-layers $Al_{12}Mg_{17}$ and Al_3Mg_2 with a thickness of 5µm is formed between the connecting surface under the optimal parameters of 600J (0.4s). When the welding time is longer (>1s), the interface liquation was found at temperatures below the eutectic reaction temperature. This can be attributed to the presence of additional elements such as Cu and Si in the AA6111 alloy. And two methods of a 100µm-thick Al cold spray coating and a thin (1µm) manganese physical vapor deposition coating have been investigated for reduce the IMC reaction rate in Al-Mg dissimilar ultrasonic welds[14]. The results show that both coatings can reduce the thickness of the IMCs layer, while the cold spray coating has a better effect, and the peak load of the welded joint reaches 2.1KN. Peng et al.[15] studied the weldability of Al6022-T43 alloy/ ZEK100-O Mg alloy dissimilar joints with a Cu interlayer using USW at varying welding energy levels. The strength of the joint with a Cu interlayer is ~35% higher than that without a Cu interlayer at an welding energy of 1500 J. As the welding energy increases, the interfacial failure occurs first at the Al/Cu interface due to the lack of adequate interface diffusion layer, and then at the Mg/Cu interface due to the presence of too thick α-Mg and Mg_2Cu eutectic structure. The results show that thicker IMCs form at the interface and lower the fracture energy. The fracture mode changes from "extraction failure" to "interface failure" as the welding energy increases. Researchers have made a lot of efforts in dissimilar welding from the optimization of process parameters, adding filler materials (It can reduce the IMC thickness, minimize the defects and increase the strength.) and establishing an IMC growth model for the USW process of aluminium alloy/magnesium alloy dissimilar metals (It can effectively predict the thickness of IMC generated in the welding interface under different process parameters)[16-18]. It can be seen from these research papers that the generated IMCs deteriorate the joint performance and the failure is mainly determined by the distribution and thickness of the IMCs, but when the size is controlled within a certain range, the generated IMCs can improve the joint performance. Therefore, to evaluate the ultrasonic welding performance of AZ31 magnesium alloy/AA6061 aluminium alloy, it is necessary to study the types, distribution characteristics and microstructure properties of the IMCs generated in the welds. AZ31 magnesium alloy/AA6061 aluminium alloy ultrasonic welding yields a small-sized weld; the generated IMCs are smaller in size, and it is difficult to obtain the performance of the weld by conventional detection methods. Nanoindentation technology is a high-resolution testing technology that by recording the continuous change in the indenter displacement and pressure load, measures the mechanical properties of the weld zone at the microscale, such as the load-displacement curve, hardness and elastic modulus in real time[19-21]. In this paper, an AZ31 magnesium alloy/AA6061 aluminium alloy was welded by ultrasonic welding. The microstructure of the weld was determined by a series of microstructure analyses. With the help of nanoindentation testing technology, the mechanical properties of the main constituent phases of the weld were obtained. Therefore, the organizational performance dependence relationship was established, and the influence of the ultrasonic welding energy on the joint performance was obtained. In this paper, the microstructure and mechanical properties of welds are comprehensively analysed. The welding properties of AZ31 magnesium alloy/AA6061 aluminium alloy and the growth behaviour of IMCs are systematically analysed. This study has broad application prospects for enriching the theoretical basis of ultrasonic welding of dissimilar metals.
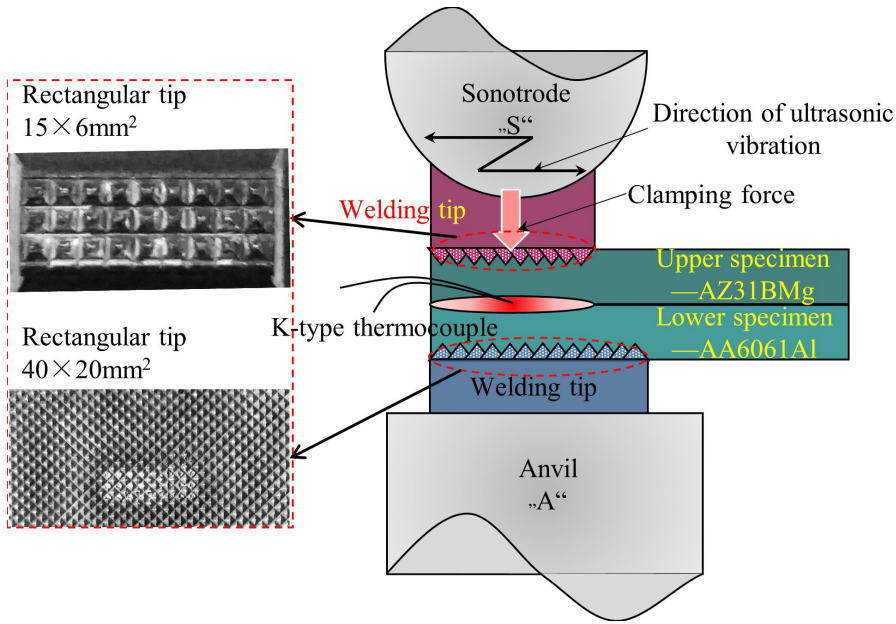
2. Experimental

In this paper, AZ31B magnesium alloy and AA6061 aluminium alloy are used for lap joint welding. The chemical compositions of the materials are shown in Table 1. The thickness of the base metal test plate is 0.5 mm. During the welding process, the sonotrode oscillates transversely along the welding direction (Figure 1). The contact pressure exerted on the sonotrode interacts with the oscillating shear forces causes dynamic internal stress at the interface between the two bonding surfaces. The USW welder used is model NC-2020A (system power P=50~2000 W, system working pressure F=460~1400 N, welding time t=0~10^4 ms, weld area 15×6 mm^2 rectangle tip with a sand grinding surface, and ultrasonic vibration frequency f=20 KHz). The main influencing parameter is welding energy. The welding parameters are as shown in Table 2. The experiment was conducted using a single factor design with 4 experimental conditions, and each experimental condition is repeated 10 times. A total of 80 specimens were prepared for mechanical performance tests to compare the effect of welding energy on joint performance. Before welding, 320# SiC sandpaper is used to remove the surface oxide of the base metal, and finally, the two materials are completely degreased with acetone.

Table 1. Chemical compositions of materials used in experiments (wt.%).

Alloy	Al	Si	Ca	Zn	Mn	Fe	Cu	Ni	Cr	Ti	Mg
AZ31B	2.9	0.08	0.04	0.8	0.6	0.003	0.01	0.001	-	-	Bal
AA6061Al	Bal	0.5	-	0.25	0.15	0.7	0.23	-	0.27	0.15	0.97

Table 2. The ultrasonic welding process parameters.

Factors	Factor name	Level
P	Welding Power (W)	1400
t	Welding Time (ms)	500, 700, 900, 1100
$E=P×t$	welding energy (J)	700, 980, 1260, 1540
F	Welding Force (N)	1150

Analysis of Microstructure and Mechanical Properties of AZ31B Magnesium Alloy/AA6061 Aluminum Alloy
Welded Joint by Ultrasonic Welding

3

Figure 1. A sketch of the ultrasonic welding equipment and sonotrode shape.

The cross-section of the weld is prepared by wire cutting. After grinding with sandpaper, the metallographic surface is finally mechanically and chemically polished by means of a SiO_2 suspension (particle size 30~40 nm). The weld microstructure is analysed by means of scanning electron microscopy (SEM, TESCAN VEGA II) and energy spectrum analysis (EDS). The phase structure of the weld is analysed by means of an X-ray diffractometer (XRD, Rigaku D/max-2400). The XRD has a step size of 0.05° (2θ) and a scan range of 30-90°. The evolution of the microtexture of the joint was analyzed by electron backscattered diffraction (EBSD) technology. During the test, the specimen tilt angle was 70°, the working distance was approximately 20 mm, and the acceleration voltage was 20 kV. The test data were analyzed using Aztec and Channel 5 software. The welding interface temperature is measured using a model AT4508 multichannel temperature tester embedded in a 0.2 mm diameter K-type thermocouple with a scan speed of 100 ms/channel. The measurement position is adjacent to the centre of the weld because the centre of the weld is the peak temperature position[22,23]. In accordance with international standard ISO 14577-2015[24], the weld performance is tested using a Hysitron Triboindenter TL-950 nanoindenter with a Berkovich indenter. The load control mode is 8 mN for the maximum load and 30 s for loading and unloading. A total of 60 test points (X × Y = 30 × 2) are set, and the test position starts from the base material AZ31B and is sequentially passed through the AZ31B-AA6061 interface and the AA6061 base material. In accordance with international standard ISO 4136-2012[25], the tensile shear (Use support plates at both ends of the lap joint, as shown in Figure 2a) and peeling strength tests (The welded joint was processed into U-bent shape using a steel jig, as shown in Figure 2b) are carried out on the specimen using a WDW3050 universal testing machine at loading speeds of 1 mm/min and 2 mm/min, respectively.

3. Results and discussion

### 3.1. The Change of the interface temperature during welding

The temperature in the weld zone increases under the surface effect and volume effect of ultrasonic welding. Accurate measurement of the interface temperature plays an important role in determining the formation phase and connection mechanism. For this reason, in the measurement process, repeated measurement experiments were performed to ensure the accuracy of the measurement peak. Figure 3 shows the peak temperature curve of the interface with different welding energies. At a welding energy of 1540 J (1100 ms), the peak temperature is 403.6 °C, which is lower than the melting point of the base material. The high strain rate plastic deformation of the metal introduces a large number of excess vacancies, which increases the Gibbs free energy and affects the thermodynamic stability. This effect causes the solid metal to melt at a temperature lower than the equilibrium melting point, and the degree of melting point reduction depends on the vacancy solubility.

3.2. Microstructures of joints

Figure 4 presents weld cross section backscattered electron (BSE) images of the AZ31B-AA6061 lap joints with weld energies from 700 J (500 ms) to 1540 J (1100 ms). The joints achieve an effective connection, and zigzag plastic deformation runs through the entire weld cross section, indicating that a mechanical interlock is locally formed. The interface IMC reaction layer changes as the welding energy increases. No significant IMC phase was observed when the welding energy was below 980 J (700 ms) (Figure 4a and 4b). At a welding energy of 1260 J (900 ms), the interface forms an IMC island and expands outward to the AZ31Mg side (Figure 4c). As the welding energy continues to increase to
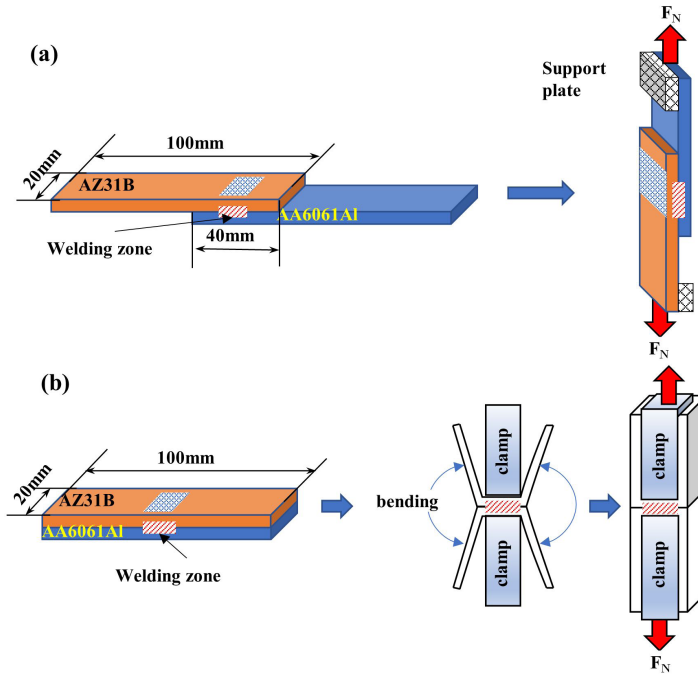
Figure 2. Schematic illustration for the tensile shear test (a) and peeling strength test of a joint (b).
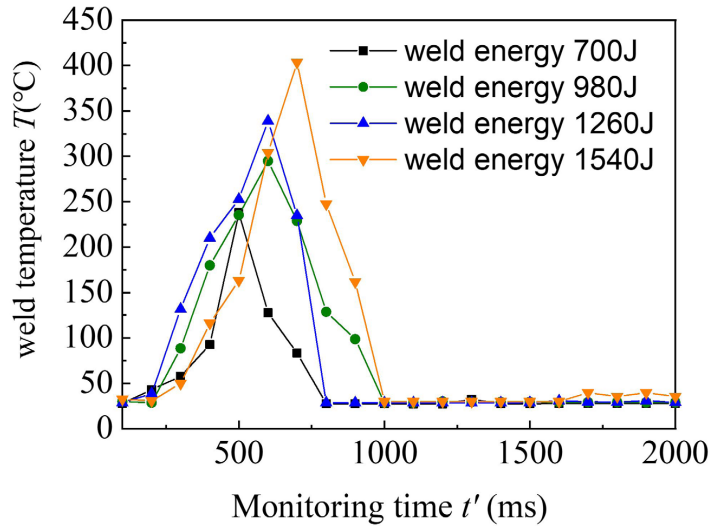
Figure 3. Peak temperature curve of the welding interface with different welding energies.

1540 J (1100 ms), the IMC island grows rapidly in the lateral direction, forming a thick continuous IMC reaction layer at the welding interface that is approximately 17 μm thick. There is evidence of melting at the weld interface, which indicates that the solid metal melts at a temperature lower than the equilibrium melting point (Figure 4d).

In order to further determine whether IMCs are formed at the welding interface and the reason for the maximum peel strength of the joint when the welding energy is 980J, the EBSD technology is used to analyze the evolution of the interface microtexture. Figure 5 shows the distribution of the EBSD inverse pole figure (IPF) of the AZ31B Mg/AA6061Al ultrasonic welding interface microstructure and the orientation

distribution function (ODF) diagram. The ODF map of 0 ° and 45 ° sections was measured to obtain the Euler angle, and the Euler angle was used to calculate the micro-textures in different regions. The average grain size of the base metal decreased from 12.4 μm (AZ31B Mg) and 23.6 μm (AA6061 Al) to 6.01 μm and 5.14 μm after welding, respectively. It shows that ultrasonic welding refines the grains at the interface[26]. The significant refinement of aluminum alloy grains is due to the fact that the face-centered cubic structure (FCC) has more slip systems than the hexagonal close-packed structure (hcp), which is easier to produce plastic deformation and achieve grain recrystallization. However, the formation of a third phase other than Mg and Al is not
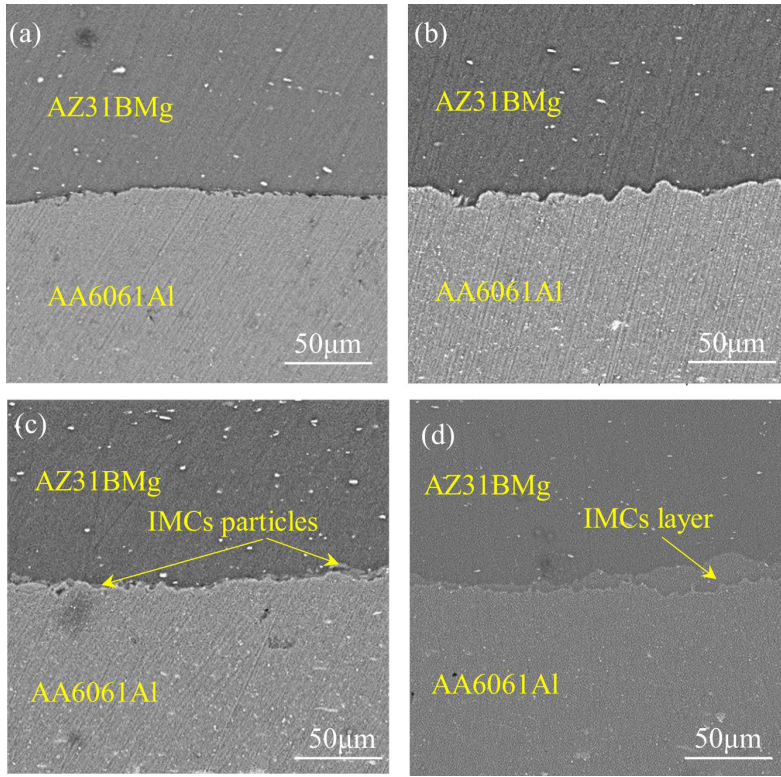
Figure 4. Microstructures of welded joints (a) 700 J (b) 980 J (c) 1260 J (d) 1540 J.
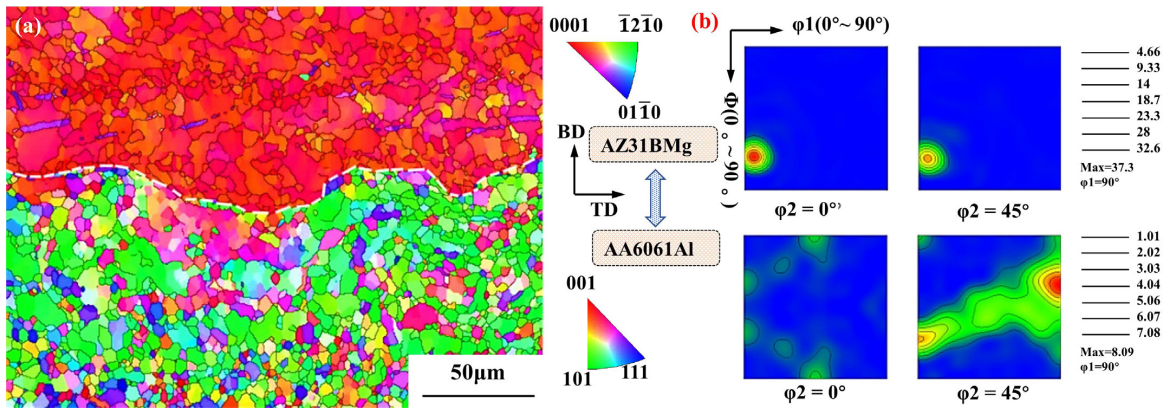

Figure 5. EBSD maps at a welding energy of 980 J (700 ms) (a) IPF (d) ODF.

found in the interface, which further indicates that no IMCs are formed in the weld. At the same time, it can be seen that there is mainly {0002}<01 1(—) 0> texture on the Mg side, and the grain orientation distribution is relatively uniform. On the aluminum side, there are mainly {100}<3 2(—) 1>, {110}<11 1(—) >, {111}<1(—) 02> strong textures, and some weak textures such as {100}<1(—) 12>, {110}<00 1(—) >, {111}<11 1(—) > et al. The strong texture Euler angles of AZ31B Mg in the 0° section are (6°, 70°, 0°), and the strong texture Euler angles of AA6061 Al in the 45° section are (90°, 30°, 45°). The evolution of interface texture is related to dynamic recovery and dynamic recrystallization mechanism during ultrasonic welding[26].

Figure 6 shows the results of an EDS line scan of the weld at a welding energy of 1540 J (1100 ms), with the scanning direction from the Mg side to the Al side of the joint. The distributions of Mg and Al are less uniform in the weld, and the sharp changes in the distributions of these elements indicate changes in the phase composition of the weld. The chemical composition of the typical phase in the weld is shown in Table 3. Baghdadi et al.[27,28] studied the effect of IMCs on the mechanical properties of the Mg/Al connection by friction stir welding solid phase joining technology. When the welding parameters are 600r/min and 40mm/min, the tensile strength of the butt joint reaches 180MPa, and the fracture along the boundary at the thermo-mechanical influence zone in the Mg side. Through EDS and XRD analysis, A thin
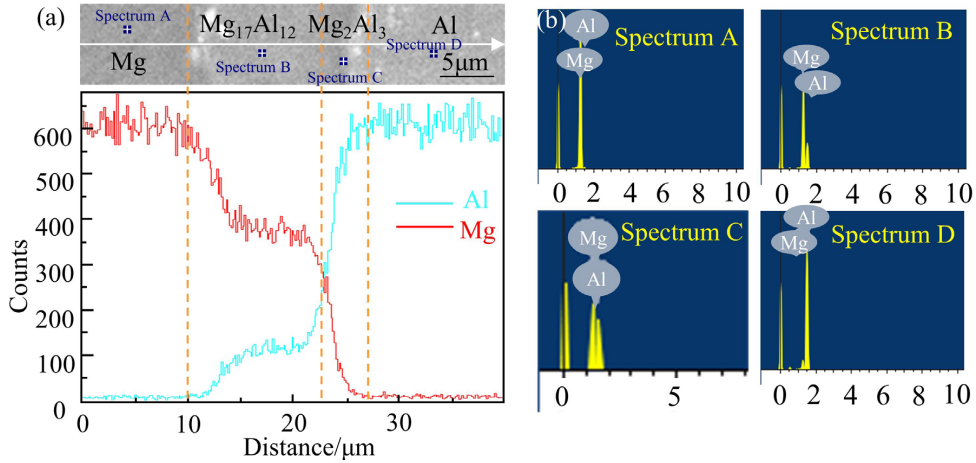
Figure 6. EDS line scan (a) and (b) point scan results of the IMC reaction layer.

Table 3. Chemical compositions and hardness of the typical phases in the weld metal (at. %).

NO.	Mg	Al	Possible phase composition	Hardness
A	97.35	2.65	Mg	0.8 GPa
B	63.13	36.87	γ-$Mg_{17}Al_{12}$	3.4 GPa
C	41.61	58.39	β-Mg_2Al_3	6.5 GPa
D	0.70	99.30	Al	1.1 GPa

layer of IMCs composed of γ-$Mg_{17}Al_{12}$ and β-Mg_2Al_3 with a thickness of less than 3.5 μm was found at the welding zone. Combined with the Mg-Al binary phase diagram[13,29], the EDS test results in Table 3 show that the IMCs are mainly composed of γ-$Mg_{17}Al_{12}$+β-Mg_2Al_3. The fracture region is examined by XRD. The results are shown in Figure 7. The presence of the γ-$Mg_{17}Al_{12}$+β-Mg_2Al_3 phase is confirmed. The XRD results are consistent with the SEM observations. The growth of IMCs during solid-state bonding occurs by diffusion, and the diffusion rate of Mg in Al is higher than that of Al in Mg, indicating that the IMCs initially formed are γ-$Mg_{17}Al_{12}$. This phase is the first to nucleate on the surface of the Al, grows to the Mg side of the weld and then grows laterally rapidly, thus forming continuous γ-$Mg_{17}Al_{12}$. Finally, a second IMC layer, β-Mg_2Al_3, is formed at the γ-$Mg_{17}Al_{12}$/Al side interface. The γ phase formation energy is -0.024 eV/atom higher than that of the β phase (-0.043 eV/atom), which indicates that the β phase growth rate is much faster than the γ phase growth rate. The hardness of the β phase is as high as 6.5 GPa, which causes this type of microstructure distribution pattern to seriously affect the toughness of the joint. At this high heat input, the Mg side γ phase undergoes a eutectic reaction ($(Mg)_{ss}$+γ-$Mg_{17}Al_{12}$↔L, 437 °C). The temperature at which the weld undergoes a eutectic reaction is lower than the eutectic temperature point of the Al-Mg binary phase diagram, which indicates that the high strain rate of the ultrasonic weld causes the weld to melt at a temperature lower than the eutectic temperature point. However, this interface melting is not synchronous, which indicates that the connection interface locally generates hot spots due to energy dissipation caused by high frequency excitation.

3.3. Mechanical properties of joints

Figure 8a shows the hardness distribution of all the test points from the nanoindentation test. The β-Mg_2Al_3 phase has the highest hardness, with an average hardness as high as 6.5 GPa. The average hardness of the γ-$Mg_{17}Al_{12}$ cubic structure phase is 3.4 GPa. The base metal AZ31 magnesium alloy and AA6061 aluminium alloy have the lowest hardnesses, and the average hardnesses of these materials are 0.8 GPa and 1.1 GPa, respectively. The observation results in Figure 4 show that the distribution of each microstructure is interphase, and thus, the hardness distribution map shows a certain area overlapping phenomenon. Figure 8b shows the load-displacement (P-h) curve for a typical phase in the weld (A-D in Table 3). The β-Mg_2Al_3 phase has a high hardness, and the indentation depth is 277.5 nm under the maximum load of 8 mN. The γ-$Mg_{17}Al_{12}$ phase has a low hardness, and the corresponding maximum indentation depth is 386.5 nm. The hardnesses of the base metal AZ31 magnesium alloy and AA6061 aluminium alloy are similar, and the corresponding maximum indentation depths are 560.0 nm and 507.5 nm, respectively. The β-Mg_2Al_3 phase shows a typical pop-in phenomenon in the P-h curve, which indicates that the material begins to plastically deform, and the deformation morphology around the indentation is similar to a shear band[30,31]. Compared with the hardness distribution of the base material, the hardness of the bonding surface has a larger variation. This is likely due to a combination of increased dislocation density, the IMCs, and residual stresses. The high strain rate and temperature gradient that occurs in the interface during the rapid connection process produces internal stresses and form IMCs. In addition, the distribution is uneven. These stresses are high enough to causes dislocation movement through local plastic deformation and/or crystal orientation gradients. Dislocation stress fields interact with each other, the existence of one dislocation will hinder the movement of the others, thereby increasing the dislocation density. The increase in dislocation density will increase the measured hardness (Taylor hardening law).

Figure 9 is a plot of the joint peak failure load of the lap shear and peel versus the welding energy. The failure load first increases and then decreases with increasing welding
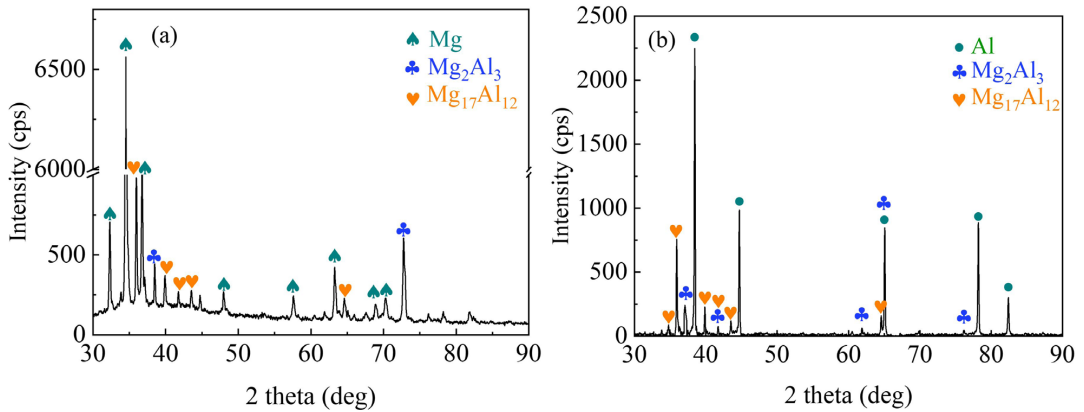
Figure 7. XRD results for welded joint fracture (a) XRD spectrum from the Mg side (b) XRD spectrum from the Al side.
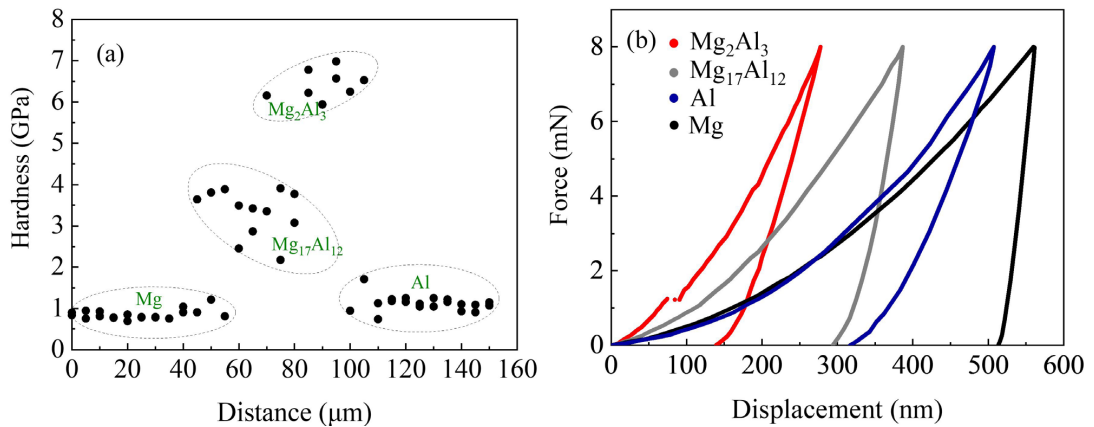

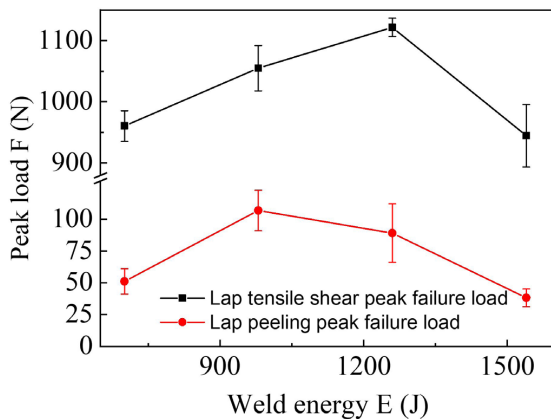**Figure 8.** Nanoindentation results for welded joint (a) Hardness distribution (b) P-h curves.

Figure 9. Lap tensile shear and peeling peak failure load test results for welded joint.

energy. The lap tensile shear peak failure load reaches a maximum of 1121.5 N at a welding energy of 1260 J, and the lap peeling peak failure load reaches a maximum of 106.9 N at a welding energy of 980 J. The results show that at low power USW (internal peak temperature <300 °C), the bonding of the workpiece is controlled by contact mechanics, and any deformation occurs on the surface of the weld. The formation of the weld initially involves ultrasonic vibrations

that disrupt the contact with the rugged surface oxide layer, resulting in localized adhesion and microconnections. In high-power welding, the best welding performance can only be obtained when the microkeys are completely bonded at the weld interface. This condition explains why the peel strength is at a maximum at 980 J, and as the welding energy increases, the interface forms the IMC island at the time of peeling and first propagates from the edges thereof, lowering the joint peel strength. In low-energy welding, the density of weld microkeys is too low, and interface failure occurs during tensile shearing. In the range of a high energy platform with welding energy up to 1260 J, the joint demonstrates the failure mode of nugget pull-out (Figure 10a). As the welding energy continues to increase, the tensile shear strength of the joint decreases rapidly, and failure occurs at the interface, which is related to the rapid growth of the β phase, the heat of the workpiece intensified (the plastic zone expands, which weakened the cross section), and the fatigue cracks generated on the surface and internally.

Figure 10b and 10c is the tensile shear failure interfacial fracture morphology of the joint welded at an energy of 980 J (700 ms) and 1540 J (1100 ms). At a welding energy of 980 J (Figure 10b), the fracture is mainly composed of a large number of layered "fish scale" small planes, and no brittle fracture characteristics are found, which indicates that the welded joints with this parameter have certain plastic
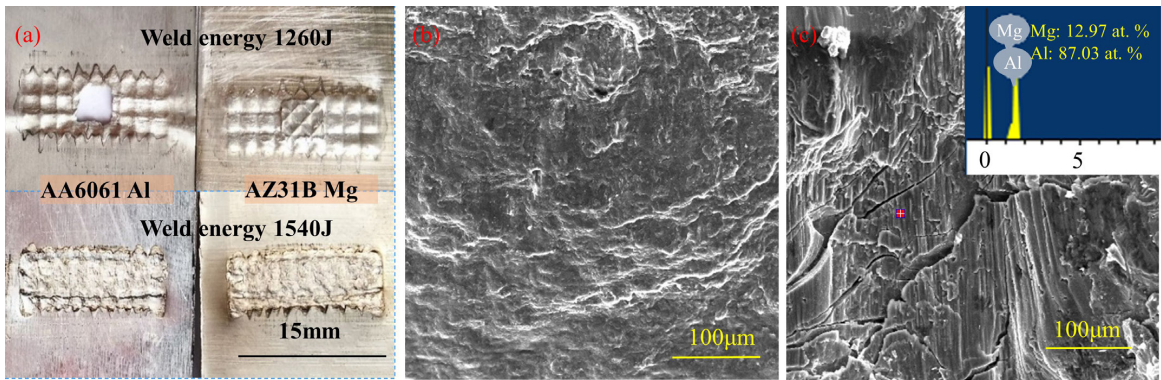
Figure 10. The failure behaviour (a) and fracture morphology of the welded metal (b) 980 J (c) 1540 J.

characteristics. At a welding energy of 1540 J (Figure 10c), the fracture surface is flat, and there are no obvious signs of plastic deformation. The fracture exhibits cleavage fracture characteristics and a large number of secondary cracks, and joint failure occurs rapidly. Combined with the EDS results, these results indicate that the surface phase is mainly composed of β phase + Al. This conclusion is drawn due to the higher hardness of the β phase and a continuous distribution state, resulting in poor toughness in the region and eventually failure in the region during tensile shearing. Therefore, the size and distribution of β-Mg_2Al_3 brittle IMCs affect the performance of the entire joint. How to refine brittle IMCs through alloying ideas is the focus of future research.

4. Conclusions

In this paper, AZ31 magnesium alloy/AA6061 aluminium alloy was used for lap joint USW. Through a series of structural properties tests, the distribution pattern of IMCs in the weld and the corresponding mechanical properties were studied. The main conclusions are as follows:

1. At a welding energy of 1540 J, the peak temperature is 403.6 °C, which is lower than the melting point of the base metal, but there is evidence of melting at the weld interface.
2. At the time of welding, the IMC island initially formed is γ-$Mg_{17}Al_{12}$, and then β-Mg_2Al_3 is formed at the γ-$Mg_{17}Al_{12}$/Al side interface and rapidly grows. The average hardness of the β-Mg_2Al_3 phase is as high as 6.5 GPa, and a typical pop-in phenomenon is observed; the average hardness of the γ-$Mg_{17}Al_{12}$ phase is 3.4 GPa.
3. The welded joint is plastic fracture at a welding energy of 980J. When the welding energy reaches 1540 J, the fracture surface is flat, and there are no obvious signs of plastic deformation.

5. Acknowledgements

6. References

1. Sahr DIC, Berger DIL, Lesemann DIM, Urban DIP, Goede DCM. Systematic material selection for the superlight-car's body-in-white. ATZ Auto Technology. 2010;10(3):22-9.
2. Goede M, Stehlin M, Rafflenbeul L, Kopp G, Beeh E. Super Light Car-lightweight construction thanks to a multi-material design and function integration. Eur Trans Res Rev. 2009;1(1):5-10.
3. Meschut G, Janzen V, Olfermann T. Innovative and highly productive joining technologies for multi-material lightweight car body structures. J Mater Eng Perform. 2014;23(5):1515-23.
4. Li ZF, Dong J, Zeng XQ, Lu C, Ding WJ, Ren ZM. Influence of strong static magnetic field on intermediate phase growth in Mg-Al diffusion couple. J Alloys Compd. 2007;440(1-2):132-6.
5. Gateman SM, Georgescu NS, Kim MK, Jung IH, Mauzeroll J. Efficient measurement of the influence of chemical composition on corrosion: analysis of an mg-al diffusion couple using scanning micropipette contact method. J Electrochem Soc. 2019;166(16):C624-30.
6. Liu W, Long L, Ma Y, Wu L. Microstructure evolution and mechanical properties of Mg/Al diffusion bonded joints. J Alloys Compd. 2015;643:34-9.
7. Zettler R, Silva A A M, Rodrigues S, Blanco A, Santos JF. Dissimilar Al to Mg alloy friction stir welds. Adv Eng Mater. 2006;8(5):415-21.
8. Yin K, Cao L, Wang N. Mechanical properties and residual stresses of 5083 to AM60B dissimilar friction stir welding with different process parameters. J Adhes Sci Technol. 2019;33(23):1-15.
9. Firouzdor V, Kou S. Formation of liquid and intermetallics in Al-to-Mg friction stir welding. Metall Mater Trans, A Phys Metall Mater Sci. 2010;41(12):3238-51.
10. Wang Y, Luo G, Li L, Shen Q, Zhang L. Formation of intermetallic compounds in Mg–Ag–Al joints during diffusion bonding. J Mater Sci. 2014;49(20):7298-308.
11. Zhu Z, Lee KY, Wang X. Ultrasonic welding of dissimilar metals, AA6061 and Ti6Al4V. Int J Adv Manuf Technol. 2012;59(5-8):569-74.
12. Watanabe T, Sakuyama H, Yanagisawa A. Ultrasonic welding between mild steel sheet and Al–Mg alloy sheet. J Mater Process Technol. 2009;209(15-16):5475-80.
13. Panteli A, Robson JD, Brough I, Prangnell PB. The effect of high strain rate deformation on intermetallic reaction during ultrasonic welding aluminium to magnesium. Mater Sci Eng A. 2012;556:31-42.
14. Panteli A, Robson JD, Chen YC, Prangnell PB. The effectiveness of surface coatings on preventing interfacial reaction during ultrasonic welding of aluminum to magnesium. Metall Mater Trans, A Phys Metall Mater Sci. 2013;44(13):5773-81.
15. Peng H, Chen DL, Bai XF, She XW, Li DY, Jiang XQ. Ultrasonic spot welding of magnesium-to-aluminum alloys with a copper interlayer: microstructural evolution and tensile properties. J Manuf Process. 2019;37:91-100.

Analysis of Microstructure and Mechanical Properties of AZ31B Magnesium Alloy/AA6061 Aluminum Alloy
Welded Joint by Ultrasonic Welding

9

16. Prangnell P, Haddadi F, Chen YC. Ultrasonic spot welding of aluminium to steel for automotive applications-microstructure and optimisation. Mater Sci Technol. 2011;27(3):617-24.

17. Robson J, Panteli A, Prangnell PB. Modelling intermetallic phase formation in dissimilar metal ultrasonic welding of aluminium and magnesium alloys. Sci Technol Weld Join. 2012;17(6):447-53.

18. Chen BQ, Xiong HP, Guo SQ, Sun BB, Chen B, Tang SY. Microstructure and mechanical properties of dissimilar welded Ti3Al/Ni-based superalloy joint using a Ni-Cu filler alloy. Metall Mater Trans, A Phys Metall Mater Sci. 2015;46(2):756-61.

19. Godoi W, Kuromoto NK, Guimaraes AS, Lepienski CM. Effect of the hydrogen outgassing time on the hardness of austenitic stainless steels welds. Mater Sci Eng A. 2003;354(1-2):251-6.

20. Barnoush A, Asgari M, Johnsen R. Resolving the hydrogen effect on dislocation nucleation and mobility by electrochemical nanoindentation. Scr Mater. 2012;66(6):414-7.

21. Vannod J, Bornert M, Bidaux JE, Bataillard L, Karimi A, Drezet JM, et al. Mechanical and microstructural integrity of nickel–titanium and stainless steel laser joined wires. Acta Mater. 2011;59(17):6538-46.

22. Haddadi F, Abu-Farha F. The effect of interface reaction on vibration evolution and performance of aluminium to steel high power ultrasonic spot joints. Mater Des. 2016;89:50-7.

23. Haddadi F, Tsivoulas D. Grain. Structure, texture and mechanical property evolution of automotive aluminium sheet during high power ultrasonic welding. Mater Charact. 2016;118:340-51.

24. International Organization for Standardization – ISO. ISO 14577: metallic materials: instrumented indentation test for hardness and materials parameters. Part 1: test method. Geneva: ISO; 2015.

25. International Organization for Standardization – ISO. ISO 4136: destructive tests on welds in metallic materials: transverse tensile test. Helsinki, Finland: ISO; 2012.

26. Su ZZ, Zhu ZQ, Zhang YF, Zhang H, Xiao QK. Recrystallization behavior of a pure cu connection interface with ultrasonic welding. Metals. 2021;11(61):1-17.

27. Baghdadi AH, Selamat N F M, Sajuri Z. Effect of tool offsetting on microstructure and mechanical properties dissimilar friction stir welded Mg-Al alloys. IOP Conf Series Mater Sci Eng. 2017;238(1):1-9.

28. Baghdadi AH, Sajuri Z, Selamat N F M, Omar MZ, Miyashita Y, Kokabi AH. Effect of intermetallic compounds on the fracture behavior of dissimilar friction stir welding joints of Mg and Al alloys. Int J Miner Metall Mater. 2019;26(10):1285-98.

29. Shin HS, de Leon M. Analysis of interface solid-state reaction on dissimilar ultrasonic spot welding of Al-Mg alloys. Met Mater Int. 2017;23(3):554-61.

30. Jian SR, Tseng YC, Teng IJ, Juang JY. Dislocation energetics and Pop-ins in AlN thin films by Berkovich nanoindentation. Materials (Basel). 2013;6(9):4259-67.

31. Mao WG, Shen YG, Lu C. Deformation behavior and mechanical properties of polycrystalline and single crystal alumina during nanoindentation. Scr Mater. 2011;65(2):127-30.